Wang, Huiqian; Guo, H. Y.; Xu, Guosheng; Leonard, A. W.; Wu, X. Q.; Groth, M.; Jaervinen, A. E.; Watkins, J. G.; Osborne, T. H.; Thomas, D. M.; Eldon, D.; Stangeby, P. C.; Turco, F.; Xu, J. C.; Wang, Liang; Wang, Y. F.; Liu, J. B.

First Evidence of Local E× B Drift in the Divertor Influencing the Structure and Stability of Confined Plasma near the Edge of Fusion Devices

Published in:
Physical Review Letters

DOI:
10.1103/PhysRevLett.124.195002

Published: 15/05/2020

Document Version
Publisher's PDF, also known as Version of record

First Evidence of Local $E \times B$ Drift in the Divertor Influencing the Structure and Stability of Confined Plasma near the Edge of Fusion Devices

H. Q. Wang,[1,*] H. Y. Guo,[1] G. S. Xu,[2] A. W. Leonard,[1] X. Q. Wu,[2] M. Groth,[3] A. E. Jaervinen,[4] J. G. Watkins,[5] T. H. Osborne,[1] D. M. Thomas,[1] D. Eldon,[1] P. C. Stangeby,[6] F. Turco,[7] J. C. Xu,[2,†] L. Wang,[2] Y. F. Wang,[2] and J. B. Liu[2]

[1]*General Atomics, Post Office Box 85608, San Diego, California 92186-5608, USA*
[2]*Institute of Plasma Physics, Chinese Academy of Sciences, Hefei 230031, China*
[3]*Department of Applied Physics, Aalto University, FI-00076, Aalto, Finland*
[4]*Lawrence Livermore National Laboratory, Livermore, California 94550, USA*
[5]*Sandia National Laboratories, Post Office Box 969, Livermore, California 94551, USA*
[6]*University of Toronto Institute for Aerospace Studies, 4925 Dufferin St., Toronto M3H 5T6, Canada*
[7]*Columbia University, 500 West 120th St., New York, New York 10027, USA*

(Received 4 October 2019; accepted 17 April 2020; published 13 May 2020)

The structure of the edge plasma in a magnetic confinement system has a strong impact on the overall plasma performance. We uncover for the first time a magnetic-field-direction dependent density shelf, i.e., local flattening of the density radial profile near the magnetic separatrix, in high confinement plasmas with low edge collisionality in the DIII-D tokamak. The density shelf is correlated with a doubly peaked density profile near the divertor target plate, which tends to occur for operation with the ion $B \times \nabla B$ drift direction away from the X-point, as currently employed for DIII-D advanced tokamak scenarios. This double-peaked divertor plasma profile is connected via the $E \times B$ drifts, arising from a strong radial electric field induced by the radial electron temperature gradient near the divertor target. The drifts lead to the reversal of the poloidal flow above the divertor target, resulting in the formation of the density shelf. The edge density shelf can be further enhanced at higher heating power, preventing large, periodic bursts of the plasma, i.e., edge-localized modes, in the edge region, consistent with ideal magnetohydrodynamics calculations.

DOI: 10.1103/PhysRevLett.124.195002

The boundary conditions at field line end are crucial in affecting plasma global behavior through manipulating the plasma edge in both nature and laboratory, such as solar corona [1,2], Z pinch [3], plasma thruster [4], linear plasma device [5], and tokamak [6]. In tokamaks, the main plasma in the closed flux surface could be strongly affected by that in the open field line and also near the wall and divertor region, such as the fueling [7] and divertor geometry effects [8]. Meanwhile, to control the boundary plasma behavior, including to control the heat and particle fluxes toward the plasma facing components, has become a critical issue for high-power steady-state fusion devices. In particular, high confinement mode (H mode), which has been adopted as the baseline operation scenario for ITER [9], features periodic bursts of plasmas known as edge localized modes (ELMs), posing increased plasma-material interaction (PMI) challenges [10,11]. Recent experiments and simulations have found that the $E \times B$ drifts driving significant particle flow in the divertor and scrape-off-layer (SOL) region play important roles on the boundary plasma dynamics, such as divertor in-out asymmetry [12] and detachment bifurcation [13].

In this Letter, we demonstrate, for the first time, that the $E \times B$ drift flow in the open-field-line plasma can act as a bridge connecting the downstream divertor and the upstream plasma, strongly affecting the pedestal structure and hence the dynamics of ELMs. The drifts first change the particle distribution in divertor and then upwardly modify the profiles of the pedestal. This, in turn, significantly affects the magnetohydrodynamic (MHD) stability at the pedestal, which leads to small ELMs, facilitating favorable integration of high-performance core with mitigated PMI in DIII-D. These findings point to an interesting path to explore for improving core-edge integration in next-step high-performance long-pulse fusion plasmas.

The experimental results are obtained from the typical DIII-D H-mode plasmas with plasma current $I_p \sim 0.9$ MA, toroidal magnetic field $B_T \sim 1.8$ T, lower-single-null shape and 4 MW neutral beam heating. Several advanced diagnostics are utilized to obtain both upstream and downstream plasma profiles, including a high-time resolution Thomson scattering system and divertor Langmuir probes. The high-spatial resolution profiles were obtained by employing the slow X-point sweeping and EFIT mapping techniques [13]. No large external resonant magnetic perturbations for ELM control were applied, but small standard error-field correction was used. All cryopumps are off in order to eliminate the effects of pumping on the profiles and particle balance.

A so-called upstream density "shelf" is evidenced by the local flattening of the radial density profile near the last closed flux surface ($\psi_n \sim 1.0$), following the steep-density-gradient region ($0.98 < \psi_n < 1.0$), as shown in Fig. 1(a) for a typical low-density H-mode plasma with ion $B \times \nabla B$ away from the lower X-point. The pedestal profiles are accumulated from 80%–99% of the ELM cycle for ~1 s of stationary conditions. No such shelf structure appears for the case with the opposite B_T direction, i.e., ion $B \times \nabla B$ pointing to the lower X-point. These profiles can be fit by using a modified hyperbolic tangent function [14], except for the density profile with shelf structure. The separatrix location is determined either by using the half width of the fitted T_e profile or from the power balance technique [15], which has been routinely employed at DIII-D. The difference between these two techniques is very small ($\Delta\psi_n < 0.005$). Hence, the density shelf resides in the near-SOL region from both techniques. Note that X-point sweeping can slightly change the separatrix location, but very slightly.

Note that a flattened density profile, or so-called "density shoulder" [16–19], was observed in tokamaks mostly at high plasma density with high-collisionality SOL and commonly associated with dissipative divertors. In contrast, the newly discovered density shelf, as mentioned, is favorable at low collisionality in the vicinity of the separatrix across the pedestal and the near SOL. It should be pointed out that no strong edge fluctuation such as the bursty-chirping mode was found to associate with the density shelf [20].

It is notable that the "shelf" is frequently observed in the plasmas with the ion $B \times \nabla B$ drift away from the X-point, as utilized for the advanced tokamak (AT) scenario [21] and I mode [22]. This indicates that it arises from certain universal physics, which may facilitate achievement of these high-performance scenarios. We find that the density shelf is connected with the doubly peaked profile of particle flux, as indicated by the ion saturation current (J_{sat}) near the outer strike point [Fig. 1(e)], for the discharge with the ion $B \times \nabla B$ drift away from the X-point. The divertor temperature T_e does not exhibit a doubly peaked profile [Fig. 1(f)]. The first peak in the J_{sat} profile is near the temperature peak, which is also the main deposition location of heat flux. The second J_{sat} peak with similar amplitude to the first peak is about 5 cm away or $\psi_n \sim 1.02$ or about 2 heat flux widths out from the strike point. Note that the double-peak structure appears at a fixed location relative to the magnetic strike point and moves along the divertor target plate following the motion of the strike point, suggesting that it is not a divertor geometry effect. This double-peak structure does not appear in the temperature or potential profiles, consistent with the assertion that it is not due to an error field. Interesting to note that in the plasma with the ion $B \times \nabla B$ drift toward the divertor, the double-peak structure is near the inner strike point, implying a B_T-direction dependence. It should be pointed out that the density shelf has been observed for years [21,23], though significant improvements of pedestal TS [24] and DTS [25] were made during recent years, which significantly increased spatial resolution.

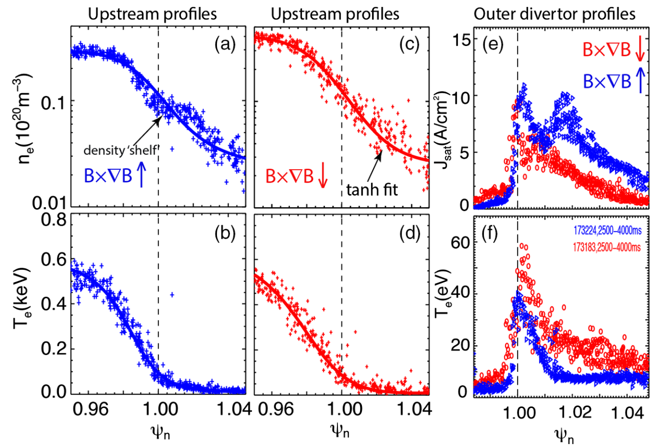

FIG. 1. Upstream profiles of electron density (a),(c) and electron temperature (b),(d), along with the profiles of ion saturation current (e) and electron temperature (f) at the outer divertor target plate, for forward (red) and reversed B_T (blue), as a function of the normalized magnetic flux function ψ_n, for a typical low-density H-mode plasma without gas puffing in DIII-D. The last closed flux surface, i.e., the separatrix, is indicated by the dashed line at $\psi_n \sim 1.0$. The ion $B \times \nabla B$ is pointing toward the lower X-point for the forward B_T. Both of the discharges shown here exhibit a high confinement quality with $H_{98} > 1.1$.

The correlation between the upstream and divertor density profiles has been identified by the presently unique divertor Thomson scattering system (DTS) in DIII-D. DTS measurement shows gradual development of the double-peak structure near the divertor target plate to the density shelf in the upstream SOL. As shown in the Fig. 2(a), the density shelf can be found in the DTS channels above the X-point in the H-mode plasmas with the ion $B \times \nabla B$ drift away from the X-point. Meanwhile, the lowest channel of DTS near the divertor plate, i.e., DTS-0, shows a clear double-peak structure [Fig. 2(b)], as already seen by the divertor probes. About 3 cm above the divertor target, DTS-1 exhibits a modest double-peak structure with a weak dip. Further upward, DTS-2 shows a single peak away from the strike point. Even further upward, DTS-3 [Fig. 2(c)] and 4–7 [Fig. 2(a)] show a gradual density decrease and become flat.

In addition, the DTS measurements show a radial propagation of the double-peak structure. Near the target plate, the first peak is around $\psi_n \sim 1.005$ and the second peak is around $\psi_n \sim 1.02$. About 3 cm above, the first peak has moved to $\psi_n \sim 1.0075$ with the second peak around $\psi_n \sim 1.015$. About 2 cm further above, the two peaks are merged into a single peak near $\psi_n \sim 1.01$. In contrast, the peak temperature locates at similar magnetic flux locations for the different DTS channels. Such poloidal and radial propagations are correlated with the complex drift flow in the divertor region, which is discussed below. It is worth noting that in the forward B_T plasmas, neither such a double-peak divertor profile nor such density shelf is found in the DTS measurements.

The underlying physics on how the $E \times B$ drifts affect the divertor plasma profiles can be further directly elucidated from the 2D measurements. The high density in the far SOL is driven by the radial $E_\theta \times B$ drift, which is supported by several 2D boundary simulation codes, e.g., UEDGE [26]. Radial diffusion flow, i.e., $V_{r,\mathrm{diff}} = -DLn_e$, is less important than the drift flow, as the density profiles are very flat. Here, D is the radial transport coefficient, and Ln_e is the density gradient scale length. The radial drift flow [Fig. 2(g)] from poloidal projection of the parallel electric field, E_θ, peaks at two regions: (1) near the peak temperature region $\psi_n \sim 1.002$ and (2) around the density dip $\psi_n \sim 1.01$. Here, with DTS measured profiles, E_θ is

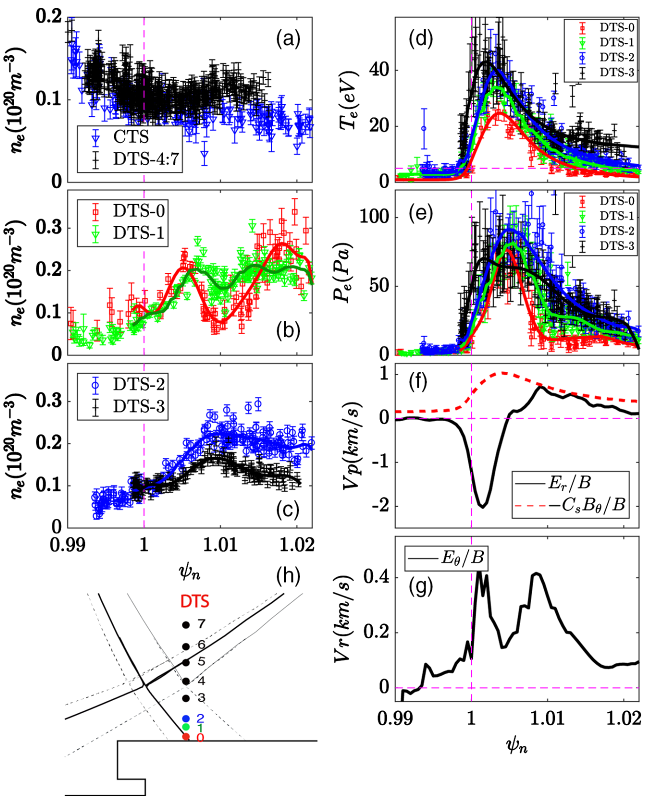

FIG. 2. Divertor profiles of the plasma with density shelf in Fig. 1. (a) Core Thomson scattering above the outer midplane (triangle), divertor Thomson scattering channels (4–7) above the X-point, (b) radial density profiles from divertor Thomson scattering channel 0 (red) and 1 (green), (c) channel 2 (blue) and 3 (black), (d) electron pressure, (e) electron temperature, (f) poloidal flow induced by radial electric field calculated from Langmuir probe (black) and poloidal projection of ion sound speed (red), (g) radial flow velocity induced by poloidal electric field calculated from DTS, and (h) DTS channels 0, 1, 2, 3 are about 0.9, 3, 5, 9 cm above the target plate, respectively. The range of X-point sweeping is also marked in (h).

calculated based on the electron momentum equation, i.e.,$E_\theta = BJ_{//}/B_\theta\sigma - 0.71\partial T_e/\partial s_\theta - \partial P_e/n_e\partial s_\theta$, where $J_{//}$ is the parallel current, σ is the plasma conductivity, B_θ is the poloidal magnetic field, and s_θ is the poloidal distance. The parallel current term can be neglected in the high temperature region due to high conductivity, and in the low temperature region due to low parallel current. The E_θ leads to a radial velocity of $V_{E_\theta \times B} \sim 0.4$ km/s, which can quantitatively explain the 4 cm radial distance of the peaks between the DTS-2 and DTS-0, i.e., $\mathrm{dr} = V_r L_{//}/C_s \sim 4$ cm with $L_{//} \sim 4$ m and assuming parallel flow velocity close to the ion sound speed $C_s = \sqrt{(T_e + T_i)/m_i}$. The poloidal electric field around the peak temperature is mainly due to the temperature gradient from parallel thermal transport, since the parallel temperature gradient correlates with the parallel heat flux $q_{//}$: $\partial T_e^{7/2}/\partial L_{//} \propto -7q_{//}/2\kappa_{0e}$.

The second peak of radial drift flow around the density dip is mainly due to the poloidal density gradient and static pressure loss. This originates from the coupling of the sheath boundary condition with the poloidal drift flow, as discussed below. The strong temperature gradient leads to significant radial electric field and thus poloidal flow. From the measurement by the divertor Langmuir probes, the positive radial electric field drives the poloidal flow [Fig. 2(f)] away from the target plate at a velocity $V_{E_r \times B} = E_r/B \sim 0.8$ km/s ($\psi_n \sim 1.01$) close to the poloidal projection of ion sound speed, $V_{E_r \times B} \sim -C_s B_\theta/B$. Based on the modified Bohm-Chrodura boundary condition at the entrance of magnetic presheath [27]: $(B_\theta/B)v_{//i} + E_r/B = (B_\theta/B)C_s$, the electrical drift flow would lead to a supersonic parallel ion flow $V_{//i}$ with Mach number about 2. Physically, the radial electric field would accelerate the plasma flow to supersonic by an increment of E_r/B_θ. From the Mach probe measurements in several tokamaks including JET [28], ASDEX-Upgrade [29], JT-60U [30], and DIII-D [31], the typical Mach number in the outer-midplane SOL is about 0.2–0.5. Take these numbers into the parallel pressure balance between the upstream and downstream [6],

$$(p_e + p_i + m_i n_i v_{//i}^2)_t = (p_e + p_i + m_i n_i v_{//i}^2)_u,$$

the static electron pressure near the target p_{et} is ~20% of upstream electron pressure assuming $T_i = T_e$ and thus the density near the target is much smaller than that of the upstream, which both quantitatively agrees with the experimental observations. The scale size of the magnetic presheath is order of ion Larmor radius, agreeing with the fact that the double-peak structure is usually only detected by the lowest channel of DTS and divertor Langmuir probes. Note that this boundary condition has been used in UEDGE [32], which has reproduced the double-peak structure with supersonic flow and strong

$E \times B$ flows in low-recycling reversed B_T plasmas, and not in the forward B_T [26].

An interpretive 2D model is developed to illustrate the impact of drifts, using experimentally measured profiles as inputs. The model starts with the ion continuity equation and parallel momentum equation [32]:

$$\partial_t n + \vec{v}_{E\times B} \cdot \nabla n + B_\theta \nabla_\theta \left(\frac{n v_{//i}}{B} \right) + \nabla \cdot (-D \nabla n) = S$$

$$m_i [\partial_t (n v_{//i}) + \vec{v}_{E\times B} \cdot \nabla (n v_{//i})] + \frac{B_\theta}{B} \nabla_\theta (m_i n v_{//i}^2 + p_i + p_e) + (\nabla \cdot \pi_i)_{//} = 0$$

where $\nabla \cdot \pi_i$ is the viscous force and small compared to other terms. Background equilibria magnetic field, upstream density, temperature, and downstream temperature profiles are used in the model to obtain the density near the target plate. The atomic processes including ionization, recombination, and charge exchange are estimated based on the Atomic Data and Analysis Structure [33] and are considered in the source term S. The electric field and parallel velocity are obtained self-consistently by solving the force balance equation, with the experimental target potential profiles as a boundary constraint. The diffusion coefficient is assumed to be $D = 5\ \mathrm{m^2/s}$ as the same order to that used in boundary fluid simulation. Parallel viscous is assumed to be classical. The perpendicular viscous term is anomalous. The diffusion and viscous terms are relatively small compared to other pressure terms. Details on this modeling will be discussed in future publications.

The particle and momentum equations are coupled through the $E \times B$ drift velocity and parallel momentum. Since the $E \times B$ drift is superimposed on the parallel ion velocity, in the vicinity of the divertor target, the strong radial electric field induced by strong radial electron temperature gradient leads to a supersonic parallel flow [Fig. 3(b), 3(e)] and digs a valley in the density profile due to an enhanced particle sink, which reproduces the experimental observed double-peak structure [Fig. 3(d)]. Upstream, as shown in Fig. 3(f), total ion flow as the sum of $E \times B$ flow and poloidal projection of parallel flow, i.e., $v_{\mathrm{pol}} = v_{E\times B} + v_{//i} B_\theta / B$, is strongly reduced at the region of peak potential gradient, i.e., $R\text{-}R_{\mathrm{sep}} = 0.05$ m, and the streamlines could not touch the divertor target plate which contributes the density dip as observed in the experiment. At a certain place above the target plate, i.e., $Z = 2$ cm in this case, the $E \times B$ flow that moves particle from divertor toward upstream is even higher than the ion sound flow. Particles are accumulated when the flow is stagnated or even reversed, which thus eventually results in a density shelf structure as observed in experiment.

Increased heating power can enhance the density shelf, as the T_e gradient and thus the electric field are driven higher. The resulting change of pedestal profiles can significantly affect the edge stability, naturally leading to small ELMs, which is key for the control of heat flux and erosion for a steady-state fusion reactor. Figure 4 compares two profiles from the AT plasmas with the ion $B \times \nabla B$ drift away from the X-point at different heating powers. These discharges are achieved in near-double-null shape with the same plasma current and B_T. Compared to the low power

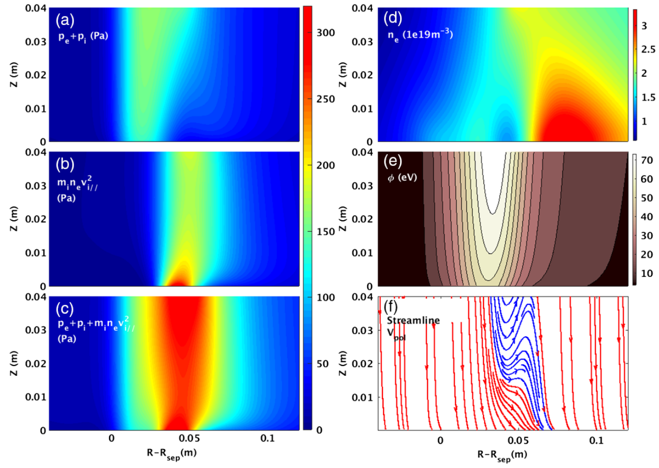

FIG. 3. Modeling results of 2D contour plot of (a) static ion and electron pressure, (b) ion dynamic pressure, (c) total pressure, (d) density, (e) plasma potential and (f) streamline of total poloidal flow. The blue lines show the stagnation of total poloidal flow at upstream.

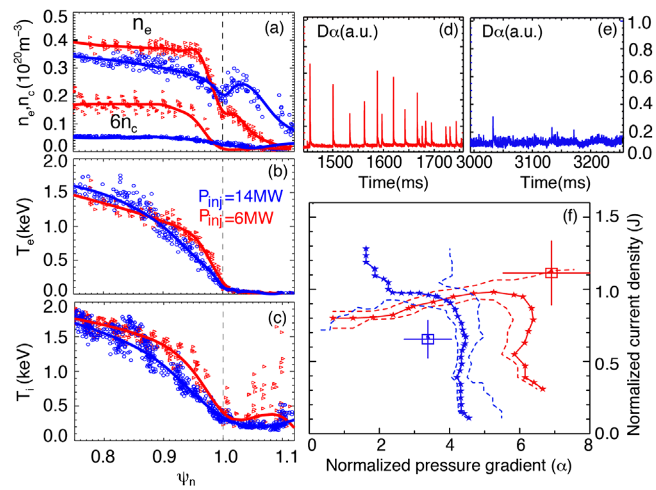

FIG. 4. Upstream profiles of (a) electron density and carbon density, (b) electron temperature and (c) ion temperature for 6 MW heating H-mode case (red) and 14 MW high heating power (blue). $D\alpha$ emission of low power with weak density shelf and large type-I ELMs (d), high-power with strong SOL density and small but high frequency ELMs (e). (f) ELITE calculations for the peeling-ballooning mode of both cases. Both cases are obtained with the ion $B \times \nabla B$ drift away from the X-point. Note that the profiles are obtained by using an 80%–99% ELM filter and accumulating within 300 ms.

(6 MW) case, high heating power significantly enhances the density shelf with the peak SOL density even comparable with that at the pedestal top [Fig. 4(a)]. At the pedestal top, the electron temperature is about 1.5 keV corresponding to a normalized collisionality of ∼0.1, which are both at the same level for ITER or fusion reactors. The main drive for the ELM crashes is from the peeling-ballooning instability [34]. Since both the pressure gradient α and edge bootstrap current density $J_{\rm bs}$ strongly correlate with the density and temperature gradients, i.e., $\alpha \propto q^2 \nabla p = q^2 \nabla (n_e T_e + n_i T_i)$ and $J_{\rm bs} \propto f(\nabla n_e, \nabla T_e, \nabla T_i)$, a low pedestal density gradient leads to a weak pressure gradient and low current density [Fig. 4(f)]. Based on the ideal MHD calculations from the ELITE code, the high-power profile is close to the ballooning boundary, resulting in a small and high-frequency ELMs [Fig. 4(e)]. In contrast, strong density gradient leads to a high pressure gradient and current density, thus triggering giant ELMs. Note that the ELITE does not include the current in the SOL [35]. However, based on previous study [36], the spontaneous equilibrium current in the SOL is relatively small and contributes little to the peeling-ballooning stability in the linear phase, which hence does not alter the onset criteria of an ELM. The small-ELM-induced energy loss is only about 0.1% of the total store energy in the high-confinement ($\beta_n \sim 3$) plasmas achieved in DIII-D. This offers an interesting regime to further explore for improving core-edge integration in next-step fusion devices.

It should be pointed out that with the assumption of constant profiles of transport coefficients in SOLPS simulation, the density pedestal gradient is expected to be weak in ITER [37], similar to the high-power case above, due to much weaker neutral fueling at pedestal. As can be seen in Fig. 4(a), even with much stronger gas puffing in the strong shelf case, both the pedestal density and density gradient are even lower than those in the low-power case. The edge impurity temperature and concentration are also lower. These suggest that the high-density SOL enhances neutral and impurity screening, thereby reduces the penetration of neutrals and impurities into the pedestal region. Therefore, the small-ELM regime with a flat pedestal density profile and simultaneously a low pedestal collisionality appears to be a natural consequence of the high-density SOL. This may be readily achievable in reactors due to the presence of an opaque SOL.

In summary, the first experimental evidence of the impact of divertor drifts on the upstream profiles in high-confinement plasmas has been obtained in DIII-D. The divertor drifts connect the doubly peaked density profile near the divertor target plate and the flattening of density profile in the upstream near-SOL. This was observed for the ion $B \times \nabla B$ drift away from the X-point, as preferred for advanced-tokamak scenarios. An interpretive model and analytical calculations from experimental data reveal that the strong drift flow leads to an enhanced dynamic pressure via coupling to the sheath boundary conditions and thus digs a valley in the divertor density profile. The drifts lead to a reversal of total poloidal flow above divertor target, producing a density shelf. High heating power can enhance the density shelf and reduce the density gradient at the pedestal, which thus significantly affects the MHD stability, producing naturally small ELMs, as observed in experiments. These findings may shed further light for the improvement of the integration between the high-confinement low-collisionality plasma and effective heat flux mitigation with small ELMs, in reactor-level plasmas.

H. Q. W. would like to thank Dr. Jose Boedo, Rich Groebner and David Hill for very helpful discussions. This work is supported by the U.S. Department of Energy under DE-FC02-04ER54698 and DE-AC04-94AL85000, National Natural Science Foundation of China under Grants No. U19A20113 and No. 11922513. DIII-D data shown in this paper can be obtained in digital format by following the links at [38].

[*]Corresponding author.
wanghuiqian@fusion.gat.com
[†]Present address: School of Mechanical Engineering, Anhui University of Science and Technology, Huainan 232001, China.

[1] R. Tavakol, E. Covas, D. Moss, and A. Tworkowski, Astron. Astrophys. **387**, 1100 (2002).
[2] V. V. Pipin and A. G. Kosovichev, Astrophys. J. Lett. **727**, L45 (2011).
[3] T. D. Arber and D. F. Howell, Phys. Plasmas **3**, 554 (1996).
[4] M. Keidar, I. D. Boyd, and I. I. Beilis, Phys. Plasmas **8**, 5315 (2001).
[5] S. C. Thakur, D. McCarren, T. Lee, N. Fedorczak, P. Manz, E. E. Scime, G. R. Tynan, and M. Xu, Phys. Plasmas **19**, 082102 (2012).
[6] P. C. Stangeby, The Plasma Boundary of Magnetic Fusion Devices (Taylor & Francis, London, 2000).
[7] A. W. Leonard, M. Groth, G. D. Porter, and M. E. Rensink, J. Nucl. Mater. **390–391**, 470 (2009).
[8] H. Q. Wang *et al.*, Nucl. Fusion **58**, 096014 (2018).
[9] E. J. Doyle *et al.*, Nucl. Fusion **47**, S18 (2007).
[10] A Loarte *et al.*, Plasma Phys. Controlled Fusion **45**, 1549 (2003).
[11] R. A. Pitts *et al.*, Nucl. Mater. Energy **20**, 100696 (2019).
[12] A. V. Chankin, J. Nucl. Mater. **241–243**, 199 (1997).
[13] A. E. Jaervinen *et al.*, Phys. Rev. Lett. **121**, 075001 (2018).
[14] R. J. Groebner, T. H. Osborne, A. W. Leonard, and M. E. Fenstermacher, Nucl. Fusion **49**, 045013 (2009).
[15] A. W. Leonard, A. G. McLean, M. A. Makowski, and P. C. Stangeby, Nucl. Fusion **57**, 086033 (2017).
[16] B. LaBombard, M. V. Umansky, R. L. Boivin, J. A. Goetz, J. Hughes, B. Lipschultz, D. Mossessian, C. S. Pitcher, J. L. Terry, and Alcator Group, Nucl. Fusion **40**, 2041 (2000).
[17] A. Wynn *et al.*, Nucl. Fusion **58**, 056001 (2018).

[18] A. V. Chankin, G. Corrigan, and C. F. Maggi, Plasma Phys. Controlled Fusion **61**, 075010 (2019).
[19] D. Moulton, G. Corrigan, J. R. Harrison, and B. Lipschultz, Nucl. Fusion **58**, 096029 (2018).
[20] T. H. Osborne *et al.*, Nucl. Fusion **55**, 063018 (2015).
[21] T. W. Petrie *et al.*, Nucl. Fusion **57**, 086004 (2017).
[22] D. G. Whyte *et al.*, Nucl. Fusion **50**, 105005 (2010).
[23] G. D. Porter, T. W. Petrie, T. D. Rognlien, and M. E. Rensink, Phys. Plasmas **17**, 112501 (2010).
[24] D. Eldon *et al.*, Rev. Sci. Instrum. **83**, 10E343 (2012).
[25] F. Glass, T. N. Carlstrom, D. Du, A. G. McLean, D. A. Taussig, and R. L. Boivin, Rev. Sci. Instrum. **87**, 11E508 (2016).
[26] T. D. Rognlien, G. D. Porter, and D. D. Ryutov, J. Nucl. Mater. **266–269**, 654 (1999).
[27] P. C. Stangeby and A. V. Chankin, Phys. Plasmas **2**, 707 (1995).
[28] S. K. Erents, R. A. Pitts, W. Fundamenski, J. P. Gunn, and G. F Matthews, Plasma Phys. Controlled Fusion **46**, 1757 (2004).
[29] M. Tsalas, A. Herrmann, A. Kallenbach, H. W. Müller, J. Neuhauser, V. Rohde, N. Tsois, M. Wischmeier, and the ASDEX Upgrade Team, Plasma Phys. Controlled Fusion **49**, 857 (2007).
[30] N. Asakura, S. Sakurai, M. Shimada, Y. Koide, N. Hosogane, and K. Itami, Phys. Rev. Lett. **84**, 3093 (2000).
[31] J. A. Boedo, G. D. Porter, M. J. Schaffer, R. Lehmer, R. A. Moyer, J. G. Watkins, T. E. Evans, C. J. Lasnier, A. W. Leonard, and S. L. Allen, Phys. Plasmas **5**, 4305 (1998).
[32] T. D. Rognlien, D. D. Ryutov, N. Mattor, and G. D. Porter, Phys. Plasmas **6**, 1851 (1999).
[33] H. P. Summers and M. G. O'Mullane, in *Nucl. Fusion Res. Underst. Plasma-Surf. Interact.* edited by R. E. H. Clark and D. H. Reiter (Springer Berlin Heidelberg, Berlin, Heidelberg, 2005), pp. 399–413.
[34] P. B. Snyder, H. R. Wilson, J. R. Ferron, L. L. Lao, A. W. Leonard, T. H. Osborne, A. D. Turnbull, D. Mossessian, M. Murakami, and X. Q. Xu, Phys. Plasmas **9**, 2037 (2002).
[35] P. B. Snyder, K. H. Burrell, H. R. Wilson, M. S. Chu, M. E. Fenstermacher, A. W. Leonard, R. A. Moyer, T. H. Osborne, M. Umansky, W. P. West, and X. Q. Xu, Nucl. Fusion **47**, 961 (2007).
[36] M. Knolker, T. E. Evans, A. Wingen, A. Bortolon, F. M. Laggner, R. A. Moyer, R. Nazikian, and H. Zohm, Nucl. Fusion **59**, 126020 (2019).
[37] M. Romanelli *et al.*, Nucl. Fusion **55**, 093008 (2015).
[38] https://fusion.gat.com/global/D3D_DMP.